Pressure-Induced Changes in Astrocyte GFAP, Actin, and Nuclear Morphology in Mouse Optic Nerve

Yik Tung Tracy Ling,[1] Mary E. Pease,[2] Joan L. Jefferys,[2] Elizabeth C. Kimball,[2] Harry A. Quigley,[2] and Thao D. Nguyen[1]

[1]Department of Mechanical Engineering, The Johns Hopkins University, Baltimore, Maryland, United States
[2]Wilmer Ophthalmological Institute, Johns Hopkins School of Medicine, Baltimore, Maryland, United States

Correspondence: Thao D. Nguyen, Glaucoma Center of Excellence, Wilmer Ophthalmological Institute, John Hopkins University, 400 N Broadway, Smith M029, Baltimore, MD 21287, USA;
vicky.nguyen@jhu.edu.

PURPOSE. To conduct quantitative analysis of astrocytic glial fibrillary acidic protein (GFAP), actin and nuclei distribution in mouse optic nerve (ON) and investigate changes in the measured features after 3 days of ocular hypertension (OHT).

METHOD. Serial cross-sections of 3-day microbead-induced OHT and control ONs were fluorescently labelled and imaged using confocal microscope. Eighteen structural features were measured from the acquired images, including GFAP coverage, actin area fraction, process thickness, and aspect ratio of cell nucleus. The measured features were analyzed for variations with axial locations along ON and radial zones transverse to ON, as well as for the correlations with degree of intraocular pressure (IOP) change.

RESULTS. The most significant changes in structural features after 3-day OHT occurred in the unmyelinated ON region (R1), and the changes were greater with greater IOP elevation. Although the GFAP, actin, axonal, and ON areas all increased in 3-day OHT ONs in R1 ($P \leq 0.004$ for all), the area fraction of GFAP actually decreased ($P = 0.02$), the actin area fraction was stable and individual axon compartments were unchanged in size. Within R1, the number of nuclear clusters increased ($P < 0.001$), but the mean size of nuclear clusters was smaller ($P = 0.02$) and the clusters became rounder ($P < 0.001$). In all cross-sections of control ONs, astrocytic processes were thickest in the rim zone compared with the central and peripheral zones ($P \leq 0.002$ for both), whereas the overall process width in R1 decreased after 3 days of OHT ($P < 0.001$).

CONCLUSIONS. The changes in structure elucidated IOP-generated alterations that underlie astrocyte mechanotranslational responses relevant to glaucoma.

Keywords: optic nerve head, GFAP, actin, IOP elevation, nucleus, astrocytes

G laucoma is an ocular disease characterized by regional visual loss owing to gradual degeneration of retinal ganglion cell axons at the optic nerve head (ONH).[1] In human and large mammalian eyes, the ONH contains supportive connective tissue beams covered by astrocytes, referred to as the lamina cribrosa (LC). Retinal ganglion cell axon bundles pass through openings between the beams and fine astrocyte processes encircle axons in LC openings. The external ONH border is delimited at the exit from the retina by Bruch's membrane opening (BMO). The astrocytic lamina in rodents, smaller by an order of magnitude in diameter than the human, is spanned by astrocytes with minimal connective tissue, but with a comparable three-dimensional network structure similar to the human. The mouse astrocytic lamina extends from the BMO to approximately 240 μm posteriorly, in an unmyelinated section of the optic nerve (ON). Further cephalad, the mouse ON axons acquire myelin. In large mammals, by contrast, myelination begins at the posterior border of the LC.

The level of IOP is a key risk factor for glaucoma; the higher the IOP, the more likely and the more severely progressive is the damage.[2] A higher IOP is accompanied by axonal degeneration, which is preceded by blockage of axonal transport in both human eyes[3] and in animal models.[4–8] The exact mechanisms linking IOP to axonal damage have not been fully delineated, but the translation of IOP into mechanical stress at the ONH has been extensively studied and modeled.[9–11] An increase in the IOP is postulated to produce trans-LC axial stress and circumferential hoop stress on the LC. Astrocytes bridge the mouse ONH and are anchored by peripheral processes to the peripapillary sclera. The structure suggests that astrocytes are important for sensing and translating mechanical stress into beneficial and pathologic events for the enclosed axons. The astrocytic network also serves to modulate ionic balance, store neuroactive substances, optimize neuronal signaling, regulate blood flow, and provide hexose nutrition to axons.[12–14] The cytoskeleton of astrocytes consists of co-existing filaments of actin and intermediate filaments.

Changes in astrocyte morphology in glaucoma models have been reported, primarily through immunolabeling of glial fibrillary acidic protein (GFAP), an intermediate filament component in astrocytes. Thickening and thinning of processes,[15,16] development of new processes along the

TABLE 1. Mouse ONs Used for Labeling of GFAP, Actin, and Nuclei

Mouse ID	Gender	Eye	Initial IOP (mm Hg)	Final IOP (mm Hg)	Difference in Final IOP (ΔIOP, mm Hg)
1	Male	Left	9	23	9
		Right	11	14	
2	Male	Left	7	22	7
		Right	10	15	
3	Male	Left	7	19	8
		Right	8	11	
4	Male	Left	8	16	8
		Right	14	8	
5	Female	Left	13	13	-1
		Right	14	14	
6	Female	Left	17	19	4
		Right	14	15	

ON axis,[17] and reorganization of filaments[18] have been shown after different time points of axonal insult. Tehrani et al[19] showed reorientation of actin-labelled rat astrocyte processes from a direction transverse to the ON axis to that along the ON axis. Both GFAP and actin contribute significantly to astrocyte stiffness and morphology, and actin is also involved with force production and vesicle mobility.[20–22] Studying the GFAP, actin, and nuclei of ONH astrocytes will likely improve knowledge of mechanisms leading to axonal degeneration.

This study provides detailed and quantitative measurement of the cytoskeletal network by analyzing fluorescently labelled mouse ON sections after 3 days of ocular hypertension (OHT), and outlining the axial and radial differences in the ON. Previous morphologic studies of astrocytes in glaucoma research have often used cultured cells or tissue sections of the ON, from which conclusions about the overall astrocytic network in the intact tissue are difficult to discern. Aligning observations relative to an anatomic reference and providing indicators for morphologic variations may aid future comparisons across studies. Serial ON sections were imaged after immunolabeling or staining for GFAP, actin, and nucleus. A custom morphologic algorithm[23] was adapted to quantify structural features, including area coverage, process thickness, and aspect ratio of the nuclei. The outcomes were used to examine differences after 3 days of OHT and to assess the effect of IOP level. Our purpose was to develop methods that will reveal alterations in mechanobiological support to axons and to advance understanding of IOP-induced mechanical changes that contribute to axonal insults.

METHODS

The following section summarizes in detail the methods in specimen preparation, image processing, and network analysis used to identify and quantify the features of the ON network structure, as well as the statistical methods for analysis of regional variations, and correlations between measured changes and degree of IOP elevation. Experimental protocols were approved by the Animal Care and Use Review Board of Johns Hopkins University School of Medicine. Mice were handled in a manner consistent with the ARVO Statement for the Use of Animals in Ophthalmic and Vision Research, and the Guide for the Care and Use of Laboratory Animals (Institute of Laboratory Animal Resources, the Public Health Services Policy on Humane Care and Use of Laboratory Animals).

Specimen Preparation

Six 6-month-old genetically modified mice expressing green fluorescent protein driven by the glutamate transporter protein 1 promoter[24] (acquired from Jeffrey Rothstein, Johns Hopkins School of Medicine[25]) were used for this study. IOP elevation was induced unilaterally by injecting microspheres consisting of 2 μL of 6 μm diameter beads, 2 μL of 1 μm diameter beads, and 1 μL of viscoelastic compound (10 mg/mL sodium hyaluronate, Healon; Advanced Medical Optics, Inc., Santa Ana, CA).[26] The fellow eyes served as contralateral controls. The IOP was measured with a Tono-Lab tonometer (TioLat, Inc., Helsinki, Finland) before bead injection and before sacrificing under anesthesia (Table 1). Anesthesia consisted of intraperitoneal injection of 75 mg/kg of ketamine, 10 mg/kg of xylazine, and 2 mg/kg of acepromazine. The difference in IOP between the 3-day treated and control eyes of each mouse was recorded as the IOP difference (ΔIOP).

For sacrifice, mice were exsanguinated under general anesthesia as detailed elsewhere in this article, then perfused with 4% paraformaldehyde in Sorenson's phosphate buffer before enucleation. The globes were immersed in the same fixative for 1 hour and were transferred into 0.1 M PO_4 buffer, where the extraocular tissues were removed. An ON segment 1 mm in length was separated from the posterior eye wall using a sharp razor blade and embedded in a mixture of 20% sucrose buffer and OCT using a modified protocol from Barthel and Raymond.[27] The cryo-embedded segment was further sectioned into 8 or 10 μm slices starting from the posterior part of the ON using Cryostat CM3050S (Leica Biosystems) at −25°C. The ON sections were collected onto glass microscope slides. Sections that were folded or torn during cryosectioning were excluded from the analysis.

Immunolabeling and Staining

For immunolabeling, ON sections were first immersed in 2% normal goat serum and 0.1% Triton X-100 in PBS solution to improve specificity and penetration of antibody. For GFAP labeling, sections were incubated with primary rabbit anti-GFAP antibody (1:1000, Abcam AB7260) overnight at 4°C in a humid chamber in the dark followed by secondary Alexa Fluor 488 goat anti-rabbit antibody
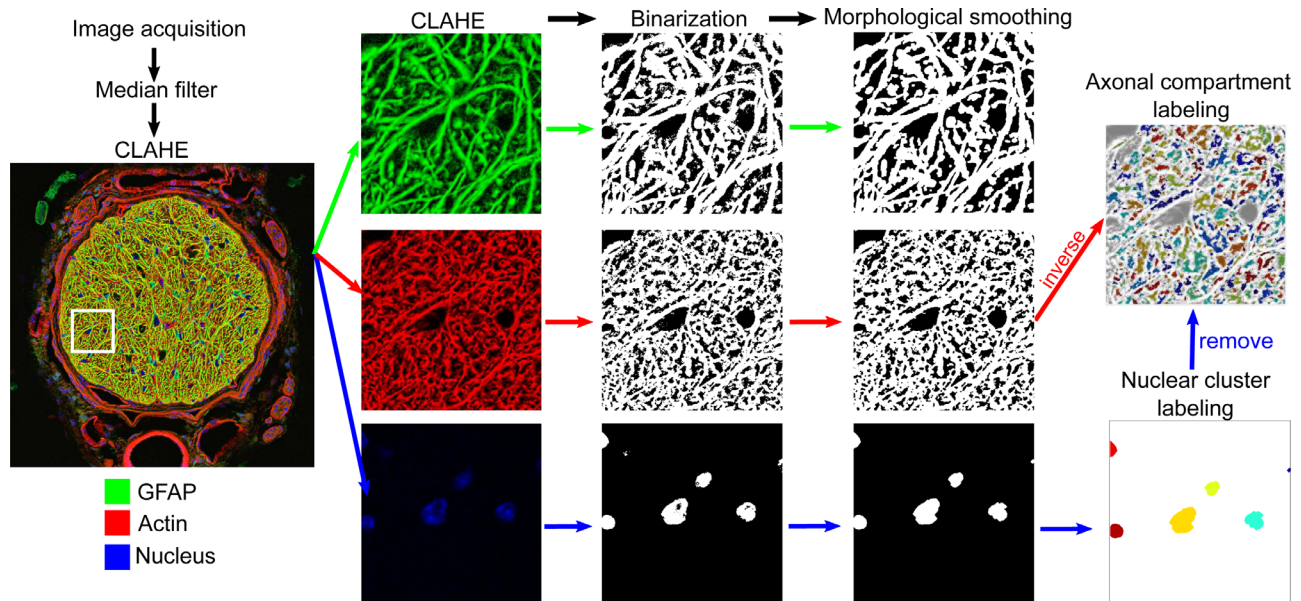
FIGURE 1. A series of image processing steps were applied to the fluorescent images to measure the features of the ON. The fluorescent image was post-processed using a median filter and contrast-limited adaptive histogram equalization and the results are shown in a 42 µm × 42 µm area for GFAP, actin and nuclear channel. Each channel was then binarized using the Otsu thresholding method[28] and morphologically smoothed. The final binarized image of GFAP channel was used for structural measurements, while those of actin and nucleus channels were further inverted to locate the axonal space. Each disconnected axonal space was randomly labelled as a separate axonal compartment and each isolated nuclear area was randomly labelled as a separate nuclear cluster for visualization.

(1:500, Invitrogen A11008; Carlsbad, CA) for 1 hour at room temperature. The ONH sections were also incubated with Alexa Fluor 568 phalloidin (1:60, Invitrogen A1280) for 20 minutes to reveal actin filaments and 4',6-diamidino-2-phenylindole (DAPI; 1:1000; Roche 10-236-276-001; Basel, Switzerland) for 1 hour for staining nuclei. All sections were mounted with Dako mounting media and covered with glass cover slips for imaging.

Image Acquisition

Confocal fluorescent images were obtained with a Zeiss LSM 710 confocal microscope using a Plan-Apochromat 40× oil-immersion objective. Three channels of images at excitation wavelength of 458 nm for GFAP, 561 nm for actin, and 405 nm for nuclei (Fig. 1) were captured for each ONH section. The z-position (depth within a section) was selected close to the surface, where signals from all three channels are visible. Each channel consisted of 3 × 3 tiled images that were stitched with a 12% overlap. The resulting images with a resolution 0.1038 µm/pixel were exported as TIFF files for structural characterization. During acquisition, the section immediately posterior to the level of retinal photoreceptor nuclei was marked as the position of BMO. Quantitative image processing was conducted on all images posterior to the BMO, which comprised ON lengths ranging from 640 µm to 960 µm.

Image Processing

Images were preprocessed with a 3 × 3 median filter to reduce noise and with contrast-limited adaptive histogram equalization[28] to enhance contrast of acquired signals (Fig. 1). All three channels were individually binarized using the Otsu thresholding method,[29] such that the actin, GFAP,

and nuclear fluorescent regions were represented as 1, and the background pixels were labelled as 0. An ON boundary was automatically detected from the binarized GFAP image by filling in spaces bounded by GFAP signals, and tracing the outermost boundary of the filled region. An average of eight sections across each ON had overestimated autotraced boundaries owing to inclusion of connecting peripapillary sclera and thus were manually corrected. The ON boundary coordinates were used to extract the area of interest in actin and nuclei channels as well. A series of morphologic smoothing was performed to remove local artifacts owing to binarization, adapted from a previously reported method.[23,30] These included using 'bwmorph' with the options of 'clean,' 'majority,' and 'bridge' to remove pixel-level noise. Morphologic opening (Matlab function 'imopen') was also applied with disk element sizes of three and diamond element size of four in the GFAP and nuclei channels, respectively, to separate regions that were partly connected. The resulting binarized images were used to measure the structural parameters in each cross-section. For verification of the binarization method, one local region of size 20 × 20 µm on the section 160 to 170 µm away from BMO of all ONs was selected for manual segmentation of the DAPI signals. Similarly, a local region of size 5 × 5 µm was manually traced on the GFAP and actin images as well. The manual segmentations were compared with that from the image processing algorithm by calculating the percentage differences in the resulting area fractions. The calculation of area fraction is described in detail in the Structural Measurements section. The image processing and structural measurement code is available on GitHub (https://github.com/trayling/Morph_Analysis).

Structural Measurements

A total of 18 structural features were measured using a custom code in Matlab R2019a (MathWorks, Inc., Natick,
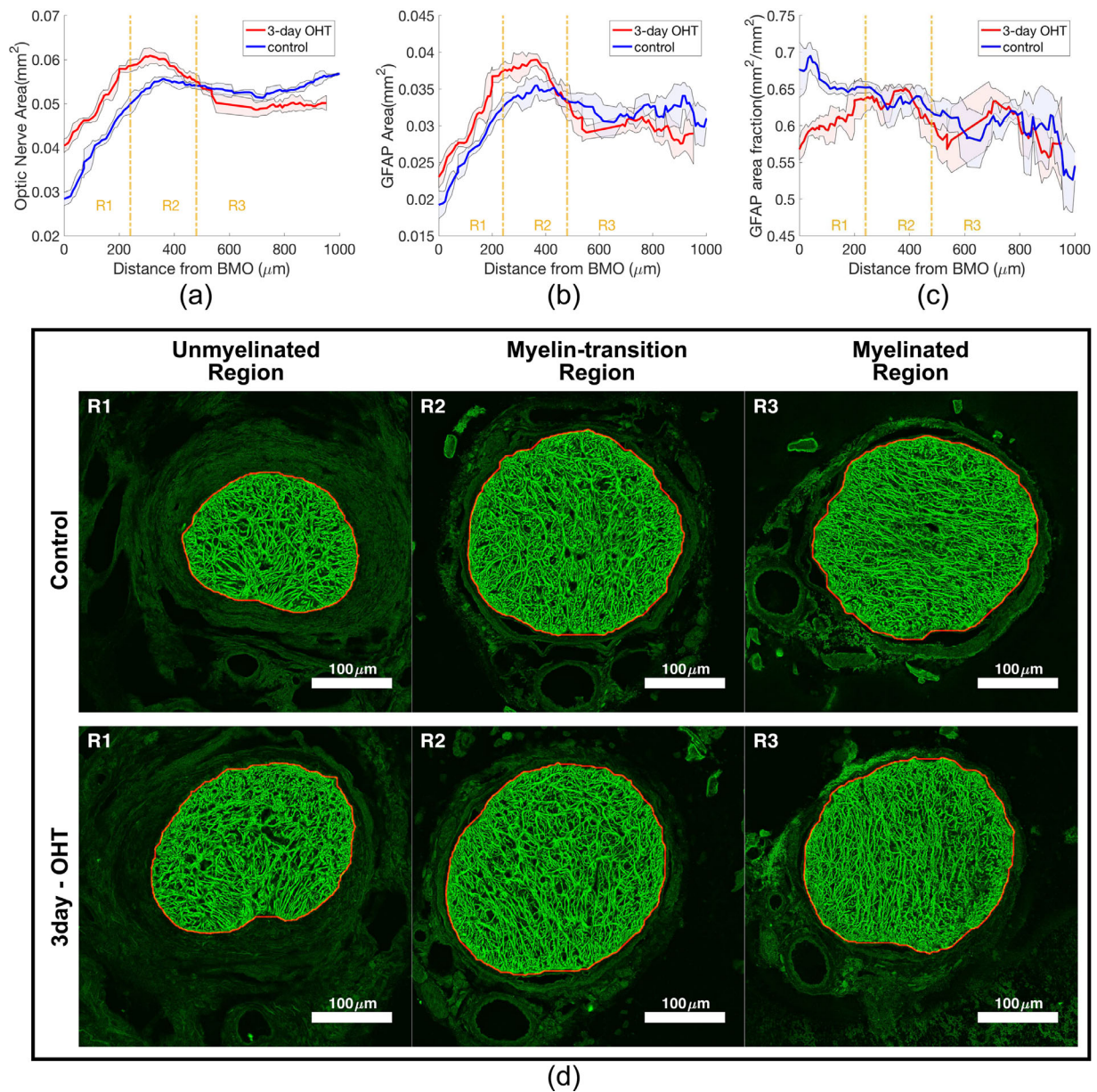
FIGURE 2. The axial variations of outcomes measured from the GFAP channel, showing the (a) ON area, (b) GFAP area, and (c) GFAP area fraction of both control and 3-day OHT measurement from representative mouse 1. The colored lines represent the moving mean of five successive sections along the ON and the shaded areas represent the respective moving standard deviations. Separation of R1, R2, and R3 corresponds with the unmyelinated, myelin-transition, and myelinated regions of the ON, respectively. (d) Representative distance-matched pairs of GFAP-labelled control and OHT ONs after median filter and contrast-limited adaptive histogram equalization were taken from each axial region of mouse 1. The mouse ON typically transitions from a kidney bean shape in R1 into an oval shape in R2 and R3.

MA): six each from GFAP and nuclei channels, three from the actin channel, and additional three from the negative space of actin and nuclei images, which represented the axonal space. The measured features were defined as follows:

- *ON area*: The total area within the detected ON boundary; the boundaries were highlighted in red lines in (Fig. 2d).
- *ON aspect ratio*: The aspect ratio was determined by fitting an ellipse to the ON boundary and calculating the ratio of the major to minor axes.

- *GFAP, actin, and nuclei area*: The total number of pixels labelled as foreground in each channel within ON boundary.
- *GFAP, actin, and nuclei area fraction*: Area fractions were recorded as the GFAP, actin, and nuclei area over the ON area.
- *GFAP process width*: Each binarized GFAP image was skeletonized using the Matlab function 'bwmorph' with options 'thin' and 'inf.' Skeletonization represents the middle line of each process with line width of 1 pixel. Process width at each skeleton pixel was measured as two times the shortest distance from the skeleton pixel to the boundary of the
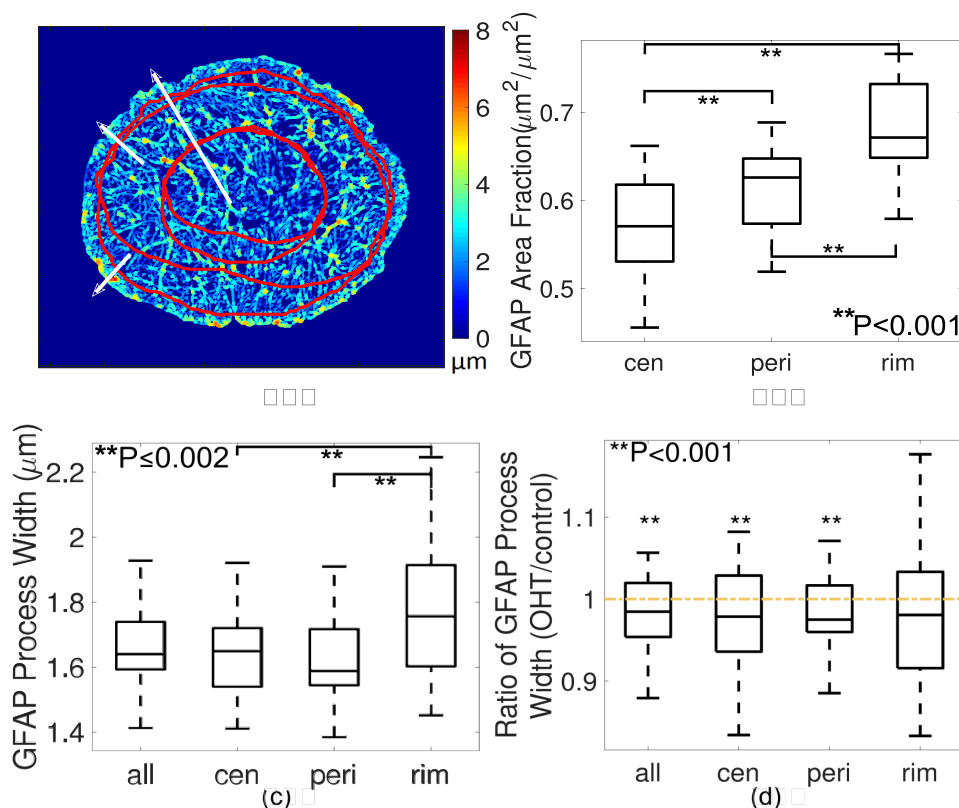
Figure 3. Radial variations in GFAP process width, showing (a) a color map of measured process width and regional divisions. Central zone (cen), peripheral (peri) and rim zone were divided as zones within 0% to 50%, 50% to 90%, and 90% to 100% of radii from fitted center of the ON to the ON boundary. (b) In R1, the GFAP area fraction was lowest in the central zone compared with that in the peripheral and rim zones. (c) Processes were thicker in the rim zone compared with central and peripheral zones ($P \leq 0.002$ for both pairwise comparisons from linear mixed model and after Bonferroni adjustment). (d) Processes became significantly thinner overall and in central and peripheral zones after 3-day OHT, but not in the rim zone ($P = 0.08$ for the rim region and $**P < 0.001$ for others).

foreground. Average process width was calculated over all skeleton pixels in the area of interest. The average beam width was calculated both within ON and in each radial regions, as described elsewhere in this article.

- *GFAP and actin process anisotropy*: A histogram of process orientations was first obtained by applying two-dimensional discrete Fourier transform to the input image and then averaging the intensities of each pixel in a line segment that corresponded to the respective orientation.[31] A circular average of process orientation was then calculated using the Matlab circular statistics toolbox developed by Berens et al.[32] The anisotropy of the processes was defined by fitting the semicircular von Mises probability density function to the histogram of orientation angles centered about the circular average orientation. The resulting dispersion parameter, which signifies the degree of alignment along the average orientation, was defined as the anisotropy.[23] A network with processes aligned in parallel with each other would yield an infinite dispersion value, while a dispersion value of 0 would indicate that the processes are not selectively aligned along any one direction in the imaging plane.

- *Number of nuclear clusters*: The number of separated regions in the DAPI-labelled channel was recorded as the number of nuclear clusters per section (Fig. 1).
- *Nuclear cluster density*: The number of nuclear clusters per square millimeter was calculated to account for change in ON area (Fig. 1).
- *Aspect ratio of nuclear clusters*: The ratio of major to minor axes of each nuclear cluster.
- *Axonal area*: The total area within the ON that was not labelled as actin or nuclei represented the axonal area.
- *Number of axonal compartments*: Number of disconnected regions in axonal area (Fig. 1).
- *Mean area of axonal compartments*: The mean number of pixels in each axonal compartment.

Regional Division

The ONs were divided lengthwise into three regions beginning at BMO. The first segment was the unmyelinated region (R1), defined by a distance of 0 to 240 µm from the BMO. The second was the myelin transition region (R2), defined from 240 to 480 µm from the BMO and the third was the myelin region (R3) defined as greater than 480 µm from the BMO (Fig. 2a). These distances were based on the positions of

TABLE 2. Comparison of 3-Day OHT and Control ON Parameters in R1

Measured Features	Control	3-Day IOP	*P*-Value
GFAP			
Aspect ratio of ON (mm/mm)	1.21 ± 0.08	1.26 ± 0.09	0.22
ON area (mm^2)	0.042 ± 0.008	0.049 ± 0.007	<0.001
GFAP area (mm^2)	0.026 ± 0.005	0.029 ± 0.005	0.004
GFAP area fraction (mm^2/mm^2)	0.62 ± 0.02	0.60 ± 0.02	0.02
GFAP Beam anisotropy	0.11 ± 0.08	0.13 ± 0.07	<0.0001
Process width (µm)	1.65 ± 0.09	1.62 ± 0.06	<0.001
Process width - central (µm)	1.64 ± 0.11	1.60 ± 0.10	<0.001
Process width - peripheral (µm)	1.61 ± 0.10	1.58 ± 0.06	<0.001
Process width - rim (µm)	1.77 ± 0.09	1.72 ± 0.10	0.08
Actin			
Actin area (mm^2)	0.028 ± 0.006	0.033 ± 0.005	<0.001
Actin area fraction (mm^2/mm^2)	0.68 ± 0.02	0.67 ± 0.02	0.11
Actin process anisotropy	0.081 ± 0.059	0.082 ± 0.046	0.38
Axon			
Axonal area (mm^2)	0.009 ± 0.002	0.011 ± 0.002	<0.001
No. of axonal compartments (*n*/cross-section)	6324 ± 2009	6996 ± 1949	0.001
Mean area of axonal compartments (µm^2)	1.56 ± 0.25	1.56 ± 0.16	1
Nuclei			
Nuclear area (mm^2)	0.003 ± 0.001	0.004 ± 0.001	0.02
Nuclear area fraction (mm^2/mm^2)	0.071 ± 0.026	0.081 ± 0.024	0.12
No. of nuclear clusters (*n*/cross-section)	86.66 ± 8.49	127.17 ± 14.05	<0.001
Nuclear cluster density (*n*/mm^2)	2134.81 ± 394.19	2665.64 ± 516.92	0.005
Mean area of nuclear clusters (µm^2)	32.25 ± 5.43	30.05 ± 3.25	0.02
Mean aspect ratio of nuclear clusters (µm/µm)	2.18 ± 0.15	2.03 ± 0.08	<0.001

Results from general linear models for mean ± standard deviation and *P* values for ratio of 3-day OHT over control different from 1, estimated ratios are listed in column 3 of Table 3. All measured areas were higher in 3-day OHT nerves.

these anatomic regions in images of both control and treated mouse ON.[33] Within each cross-section, the ON was further divided into three radial zones: the central, peripheral, and rim zones (Fig. 3a). The zones were defined by first locating the center of mass of the ON, and then separating the ON by distances that were equal to 50% and 90% of the length from the center to the ON outer boundary.

Statistical Analysis

The structural parameters (Table 2) measured from each ON section were averaged every 40 µm interval from BMO up to 640 µm distally, amounting to six intervals each in R1 and R2, and four intervals in R3. A total of nine intervals (4.7% of all intervals) had artifact that precluded analysis of the GFAP signals. Four of these intervals had corresponding actin and DAPI signals that were similarly affected and were excluded from further analysis. To eliminate the intermouse variations in control measurements, the ratio of 3-day OHT over control eyes was calculated for each outcome in each interval to represent the fold change after treatment. A ratio of 1 indicated that the outcome was the same between treated and control nerves and a ratio of greater than 1 indicated an increase in the outcome in 3-day OHT eyes. The interval ratios were used to compare differences in structural outcomes after 3-day IOP elevation. In addition, we assessed the effect of the estimated IOP difference on the ratio in region R1. Both analyses used general linear models, which took into consideration the possible correlations among repeat ratios in multiple intervals for a single ON. The repeat measurements were assumed to have an autoregressive correlation structure, for example, the closer two intervals are in distance from the retina, the higher the correlation. The GFAP and actin network were mostly isotropic, with anisotropic dispersion values close to 0, leading to ratio values that were much greater than 1.47 fold, the median of all anisotropy ratio values. Therefore, anisotropy ratios that were more than four-fold were removed as outliers (9 intervals from GFAP and 10 intervals from actin), while the new median ratio value of 1.35-fold remained at a similar level.

For comparison of GFAP process width among central, peripheral and rim zones, all estimates and *P*-values were obtained from mixed linear models to account for the clustering of areas within each ON for a control eye, as well as correlations among intervals. Again, intervals were assumed to have an autoregressive correlation structure. Bonferroni adjustment was implemented for *P*-values from multiple pairwise comparisons. All aforementioned analyses were performed using SAS 9.2 (SAS Institute, Cary, NC). In addition, to compare the differences among ON, actin, GFAP, axonal and nuclear areas (Fig. 4a), as well as between their area fractions in R1, one-way ANOVA followed by Bonferroni correction (Matlab function *'anova1'* followed by *'multcompare'*) was used for the multiple pairwise comparison test.

RESULTS

Measured Features in Control Eyes

In control nerves, the ON, GFAP, and actin areas were smallest at the BMO. All three areas increased dramatically through R1, peaked in R2, and decreased slightly in R3 (Figs. 2a, 2b, and 5a). The GFAP area fraction in control nerves was greatest at BMO and declined through the length of ON (Fig. 2c). The actin area fraction increased steadily though R1 and remained at a similar level in R2 and R3 (Fig. 5b). The actin channel showed more distinct and
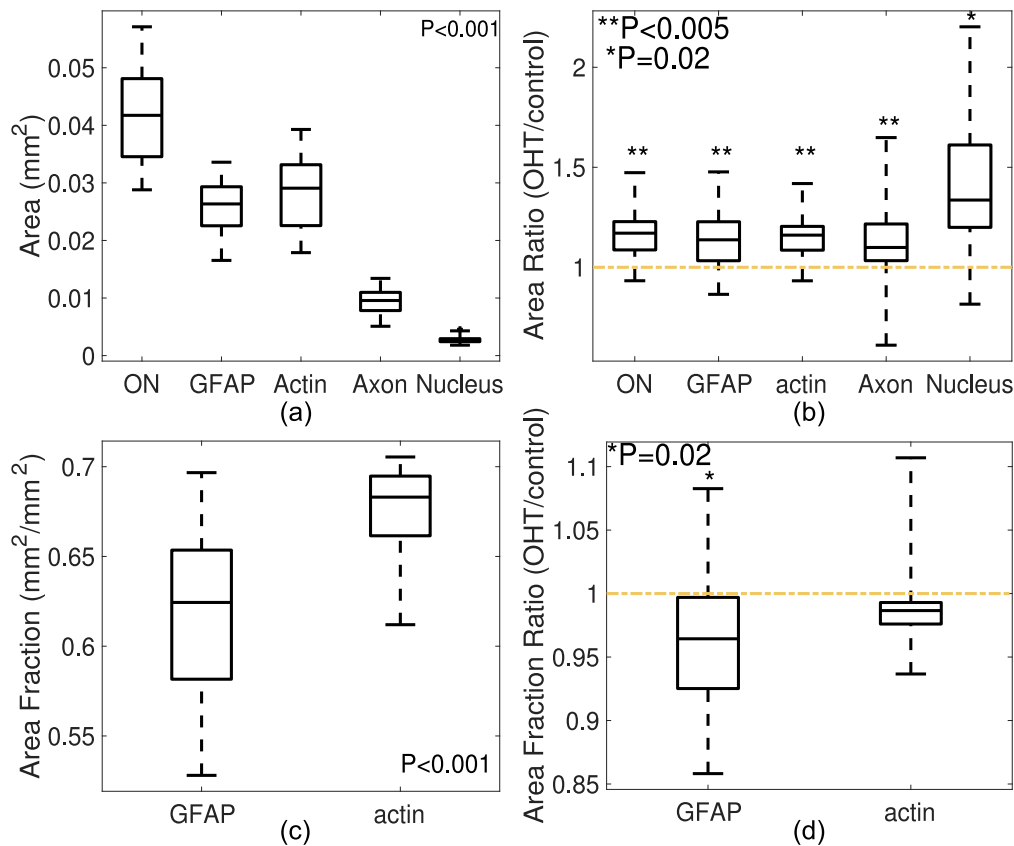
FIGURE 4. Comparison of parameter areas and area fractions (region R1) in control (left graphs) and change as a ratio between 3-day OHT and control ONs (right graphs). (a) Nuclear area is lowest compared with actin, GFAP and axonal areas ($P < 0.001$, 1-way ANOVA after Bonferroni correction). (b) All areas in R1 were greater in 3-day OHT ONs than in controls (ratio > 1). Nuclear area had the largest percentage increase (37%) after 3 days. (c) Control GFAP area fraction was lower than actin area fraction ($P < 0.001$, 1-way ANOVA). (d) There was a significantly greater percentage decrease in GFAP area fraction over the change in actin area fraction after 3-day OHT treatment. P-values for (b) and (d) were recorded from general mixed models.

elongated bundles in R1, and the actin staining in R2 and R3 had less distinct bundles (Fig. 5d–f and Supplementary Fig. S1). The total number of nuclear clusters increased from BMO through the myelinated region (Fig. 5c and Supplementary Fig. S2), and the number of axonal compartments increased steadily in R1 and R2, but became stable in R3. All cross-sectional structural outcomes were averaged 40-μm intervals and separated into axial regions of R1, R2, or R3 (Table 2 and Supplementary Tables S1 and S2) for comparison after 3-day OHT.

For ON sections in the unmyelinated region R1 of control eyes, the average ON area was 0.042 ± 0.008 mm², whereas the GFAP and actin areas covered 62% and 68% of the ON area (Fig. 4c). The average number of nuclear clusters within the ON was 86.7 ± 8.5 per section, covering 7.1% of the ON area. The axonal compartments occupied 21% of the ON area (Fig. 1). The average astrocyte process width measured from the GFAP channel was 1.65 ± 0.09 μm. Overall, astrocyte actin coverage in ON sections was greatest, followed by the GFAP, axonal area, and nuclear area ($P < 0.001$, Fig. 4a).

The average GFAP process width in the central zone of ONs in R1 was 6.7% thinner than in the rim zone, and in the peripheral zone processes were 8.4% thinner than in the rim zone ($P \leq 0.002$ for both comparisons; Figs. 3a and 3c). The GFAP area fraction in the central zone (57.5%) was also lower than in the peripheral (61.6%) and the rim zone (68.4%; $P < 0.001$ for both comparisons; Fig. 3b).

Change in Parameters After 3 Days of OHT Treatment

Across all measured features, the ratios between 3-day OHT and control nerves were similar between R2 and R3, whereas changes in R1 were most significant (Table 3), including increases in OHT ON area, actin area, and axonal area and a decrease in GFAP area fraction. The increase in number of nuclear clusters and decrease in aspect ratio of the clusters were also larger in R1 than R2 ($P \leq 0.02$ for both). Thus, we present in detail only results in R1 after 3 days of OHT treatment (Table 2).

The estimated mean areas of ON, GFAP and actin were 1.16, 1.12, and 1.15 times larger, respectively, for the 3-day OHT group than controls ($P < 0.01$, Fig. 4). In addition, the axonal area and nuclear area were 1.13 ($P < 0.001$) and 1.27 times larger ($P = 0.02$) (Table 2). Because the increase in the GFAP area was proportionally less than that of the ON area, there was a 5.3% decrease in GFAP area fraction ($P = 0.02$). The actin and nuclear area fractions remained unchanged. The GFAP process width decreased from 1.65 μm to 1.62 μm ($P < 0.001$), and the percentage decrease in central zone (3.7%, $P < 0.001$) was larger than that in the peripheral zone (2.5%, $P < 0.001$; Fig. 3c). Processes in the rim region were 2.1% thinner, but the observation was not significant ($P = 0.08$). The number of individual axonal compartments was 1.13 times larger ($P = 0.001$), but the
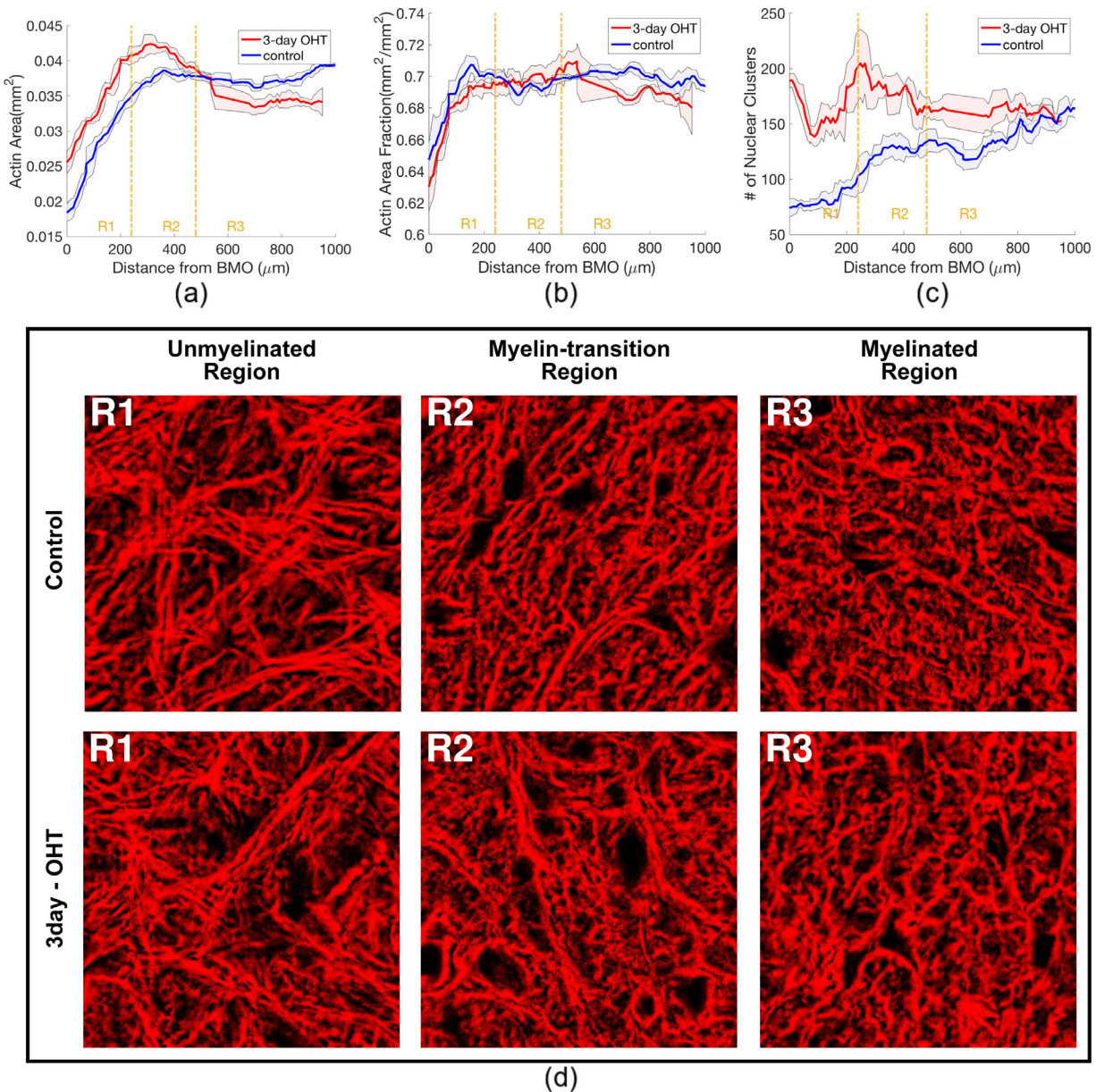
FIGURE 5. The axial variations of outcomes measured from the actin and nucleus channels, showing the (a) actin area, (b) actin area fraction and (c) number of nuclear clusters of both control and 3-day OHT measurement from representative mouse 1. The colored lines represent the moving mean of five successive sections along the ON and the shaded areas represent the respective moving standard deviations. Region R1, R2, and R3 correspond with the unmyelinated, myelin-transition, and myelinated regions of the ON, respectively. (d) A 42 μm × 42 μm area of distance-matched pairs of control and 3-day OHT actin networks after median filter and contrast-limited adaptive histogram equalization were taken from each region of the mouse 1. The actin fiber bundles were straighter and more distinct in R1 than in R2 and R3, where they take on a wavier appearance.

average area of axon compartments remained the same at 1.56 μm². The number of nuclear clusters increased from 87 to 127 per cross-section ($P < 0.001$), whereas the mean cluster area decreased by 6.8% ($P = 0.02$). On average, nuclear clusters were less elongated; their aspect ratio decreased from 2.18 to 2.03 μm/μm ($P < 0.001$, Fig. 6). The GFAP processes were aligned more in parallel with each other after 3 days of OHT, with an average dispersion of 0.11 in controls compared with 0.13 in OHT nerves (0 = completely isotropic; $P < 0.001$). The actin-labelled processes alignment and ON aspect ratio were not significantly different after 3 days of OHT treatment.

Morphologic Changes Were Associated With Difference in the Final IOP

The ratios of 3-day OHT over control data in several measured parameters were correlated with the difference in IOP between 3-day OHT and control pairs (Supplementary Table S3). The enlargement of ON area increased with greater ΔIOP (Fig. 7a). Similarly, the fold increase in GFAP area, and in number of axonal compartments also increased with increased ΔIOP (Figs. 7b and 7c). In contrast, the GFAP processes in the central zone were thinner with a larger ΔIOP (Fig. 7d).

TABLE 3. Results From General Linear Models for Comparison of Measured Outcomes Among Axial Regions

Measured Features	Estimated Mean Ratio (95% CI)			Adjusted *P*-Value	
	R1	R2	R3	R1 vs R2	R2 vs R3
GFAP					
Aspect ratio of ON (mm/mm)	1.05 (0.97–1.12)	1.03 (0.97–1.09)	1.00 (0.95–1.05)	NS	NS
ON area (mm^2)	1.16 (1.10–1.22)*	1.07 (1.03–1.11)*	1.05 (1.02–1.09)*	<0.0003	<0.0003
GFAP area (mm^2)	1.12 (1.04–1.20)*	1.09 (1.00–1.17)*	1.07 (0.99–1.14)	NS	NS
GFAP area fraction (mm^2/mm^2)	0.96 (0.93–1.00)*	1.00 (0.96–1.05)	1.00 (0.95–1.04)	0.01	NS
GFAP beam anisotropy	1.51 (1.32–1.71)*	1.89 (1.39–2.39)*	1.56 (1.04–2.08)*	0.08	NS
Process width (μm)	0.97 (0.96–0.98)*	0.98 (0.96–1.01)	0.98 (0.94–1.02)	NS	NS
Process width - central (μm)	0.96 (0.95–0.98)*	0.99 (0.94–1.03)	0.97 (0.92–1.02)	NS	NS
Process width - peripheral (μm)	0.97 (0.96–0.99)*	0.99 (0.96–1.02)	0.98 (0.94–1.02)	NS	NS
Process width - rim (μm)	0.98 (0.96–1.00)	0.98 (0.94–1.02)	0.96 (0.90–1.03)	NS	NS
Actin					
Actin area (mm^2)	1.15 (1.09–1.20)*	1.07 (1.03–1.11)*	1.05 (1.01–1.09)*	<0.0003	<0.0003
Actin area fraction (mm^2/mm^2)	0.99 (0.98–1.00)	0.995 (0.991–0.998)*	1.00 (0.99–1.01)	NS	NS
Actin process anisotropy	1.13 (0.84–1.41)	1.69 (1.14–2.24)*	1.40 (1.11–1.69)*	NS	NS
Axon					
Axonal area (mm^2)	1.13 (1.06–1.20)*	1.04 (1.00–1.08)*	1.06 (1.00–1.12)	0.002	0.05
No. of axonal compartments (*n*/cross-section)	1.13 (1.05–1.21)*	1.07 (0.98–1.15)	1.05 (0.94–1.15)	NS	NS
Mean area of axonal compartments (μm^2)	1.00 (0.90–1.10)	1.99 (0.89–1.11)	1.04 (0.90–1.17)	NS	NS
Nuclei					
Nuclear area (mm^2)	1.27 (1.04–1.51)*	1.19 (1.02–1.36)*	1.16 (1.04–1.28)*	NS	NS
Nuclear area fraction (mm^2/mm^2)	1.13 (0.97–1.29)	1.10 (1.00–1.20)	1.07 (0.97–1.17)	NS	NS
No. of nuclear clusters (*n*/cross-section)	1.38 (1.18–1.58)*	1.30 (1.13–1.47)*	1.25 (1.12–1.37)*	0.02	NS
Nuclear cluster density (*n*/mm^2)	1.19 (1.06–1.33)*	1.19 (1.08–1.31)*	1.15 (1.05–1.24)*	NS	NS
Mean area of nuclear clusters (μm^2)	0.93 (0.88–0.99)*	0.92 (0.90–0.95)*	0.98 (0.94–1.01)	NS	NS
Mean aspect ratio of nuclear clusters (μm/μm)	0.93 (0.91–0.96)*	0.99 (0.98–1.00)	1.00 (0.98–1.03)	<0.0003	0.002

Results showing the mean ratios of 3-day OHT over control outcomes and the Bonferroni adjusted *P*-values for pairwise ratio comparisons. ON, GFAP, actin and nuclear area had ratios significantly higher than 1 in all axial regions. The ratios were higher in R1 than R2 and were not significantly different between R2 and R3.

Pairwise ratio comparisons with *P* values that were not significant were marked as NS. In columns 3–5, ratio values significantly different from 1 were highlighted with *for *P* values of ≤0.05.

DISCUSSION

This study presented differences in normal astrocyte structure between the region closer to the eye (R1) and ON regions more cephalad. In controls, the GFAP area fraction and GFAP-labelled process width were greatest at BMO and both decreased toward the myelinated ON. This finding could be caused in part by the addition of oligodendrocytes and myelin in regions R2 and R3; however, the decrease in the GFAP fraction was already evident within R1, before any myelination. In R1 of control mouse ON, the average cross-sectional area was 0.042 mm^2, with an average of 87 nuclear clusters per section. Both of these are consistent with the mean area of 0.04 to 0.06 mm^2 and with a mean number of 41 to 275 nuclei reported in Swiss black mice.[34] The measured GFAP process thicknesses in R1 were slightly higher than the 1.30 μm reported by Lye-Barthel et al.[35] We measured the average thickness of all GFAP processes, including those bordering the peripapillary sclera, whereas Lye-Barthel et al.[35] measured only the thickness of 50 processes at a distance of 10 to 15 μm from the nucleus. The discrepancies could also be due to differences in animal models and strains of mice.

The control ON, GFAP, and actin areas increased throughout the unmyelinated region R1, but were relatively uniform in regions R2 and R3. The actin bundles and GFAP processes in R1 seemed to span across the entire width of the ON, forming a network in the plane of the ON cross-section. The interlacing process network in each ON cross-section was similar to the honeycomb architecture of the astrocytic network reported by Sun et al.,[36] resembling the connective tissue beam-pore network structure in the human LC, the load bearing tissue at the ONH that protects retinal ganglion cell axons. The actin processes seemed to be more convoluted in regions R2 and R3, coinciding with a more curved connective tissue pattern in the myelinated human ON.[37] After 3 days of OHT, the actin network in R1 remained isotropically arranged in the cross-section. Because actin is known to extend fibers to align with the direction of load, this suggested that the in-plane stresses experienced by the actin network were more dominant than the out of plane stresses directly contributed by the trans-laminar pressure gradient.

The 3-day OHT nerves had greater ON, GFAP, actin, axonal, and nuclear areas in R1, R2, and R3, but the increases were markedly greater in the unmyelinated R1 region. The increase in the ON area in R1 was also demonstrated in a prior study.[38] In addition, the OHT nerves in R1 exhibited a decrease in the GFAP area fraction, decrease in process width, increase in the number of axonal compartments, and increase in axonal area. Greater IOP elevations relative to the baseline produced greater morphologic changes in R1. Larger study groups with more detailed IOP measures over longer periods are needed to verify the associations between IOP elevation and the extent of remodeling in the astrocytic lamina. An increase in the IOP would subject the astrocytic lamina to a greater translaminar pressure gradient and a greater hoop stress in the eye wall. The effect would be larger in R1 than in R2 and R3, which may explain why greater remodeling of the astrocyte network structure was
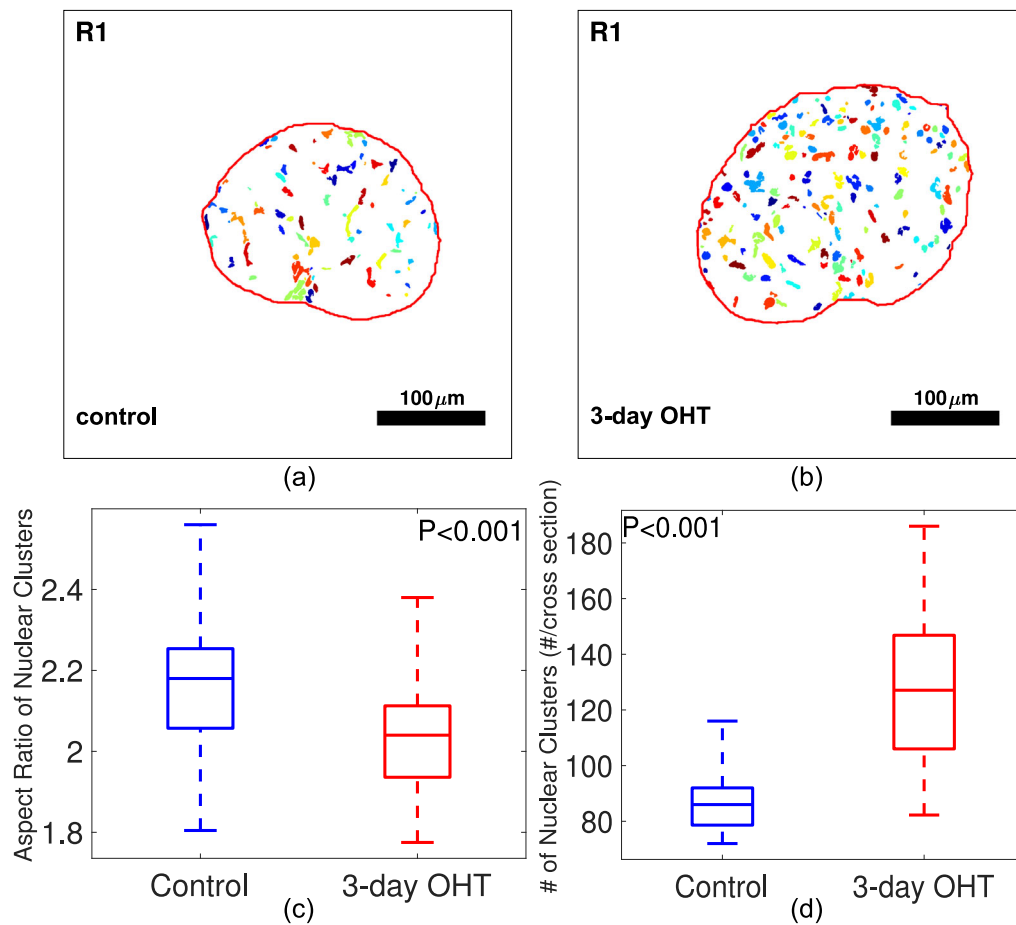
FIGURE 6. Comparison of nuclear clusters from a region-matched pair of ON sections, showing individually labelled nuclear clusters of (a) 3-day OHT and (b) control nerves. The 3-day OHT ON had (c) a higher number of nuclear clusters, but (d) a lower aspect ratio of clusters in R1.

measured in R1. R1 is also the region where axonal transport is blocked in mice.[7,39–41] Similarly, in larger mammalian eyes and humans, transport block in axons occurs in the connective tissue zone of the LC and myelination begins just posterior to this.[3,42–44] The accumulation of amyloid precursor protein[33] during axonal obstruction can lead to axonal swelling,[39,45] resulting in the increase in axonal area measured in this work.

Not only was the astrocytic network structure different from R1 to R2 and R3, it also differed quantitatively between the central, peripheral, and rim zones of the mouse ONH in control eyes. GFAP-labelled processes were thickest in the rim zone when compared with the periphery and center of the control ON in R1. The thickness of processes in the central and peripheral zones decreased significantly in the 3-day OHT nerves, but remained unchanged in the rim zone. The thicker rim zone processes contact their basement membranes adjoining the peripapillary sclera. Recent work using transmission electron microscopy[46] also showed that processes in the rim zone normally are wider, forming shapes similar to the base of doric pillars. At this site, they form electron dense junctional complexes that are integrin- and dystroglycan-linked through the cell membrane to the actin network, altering its configuration as a response to mechanical stress. Larger processes in the rim zone may provide greater structural reinforcements against loading

from translamina pressure gradient and the scleral hoop stress. This finding was consistent with our finding that IOP-induced strain responses were greater in the central ON of mice than in the periphery with ex vivo inflation testing.[47]

Studies of astrocytes in culture have shown that mechanical stress can increase the production of GFAP[48] and upregulate the expression of intermediate filaments.[49] The GFAP area was greater in R1 of the 3-day OHT eyes, which may be a result of the stress-stimulated GFAP production. However, previous studies of mouse and rat glaucoma models did not find an increase in GFAP gene expression.[16,50,51] In rat glaucoma, GFAP was reportedly downregulated.[52] Thus, the increase in GFAP area may be caused by a redistribution of overlapping processes, although the effect on the GFAP area was not proportional to the enlargement of ON area, which caused the area fraction to decrease. A redistribution of filaments after an increase in hydrostatic pressure has also been reported in cultured human astrocytes.[53]

Rearrangement of the actin cytoskeleton stimulated by hydrostatic pressure or other forms of mechanical stress is known to be a mechanotranslational response in different cell types.[19,54–56] In neurodegenerative diseases, actin reorganization occurs[57] and in experimental and human glaucoma, astrocytes move to fill ONH pores previously occupied by axons.[1] Although axonal loss is not present within 3 days in the bead injection model, actin reorganization may
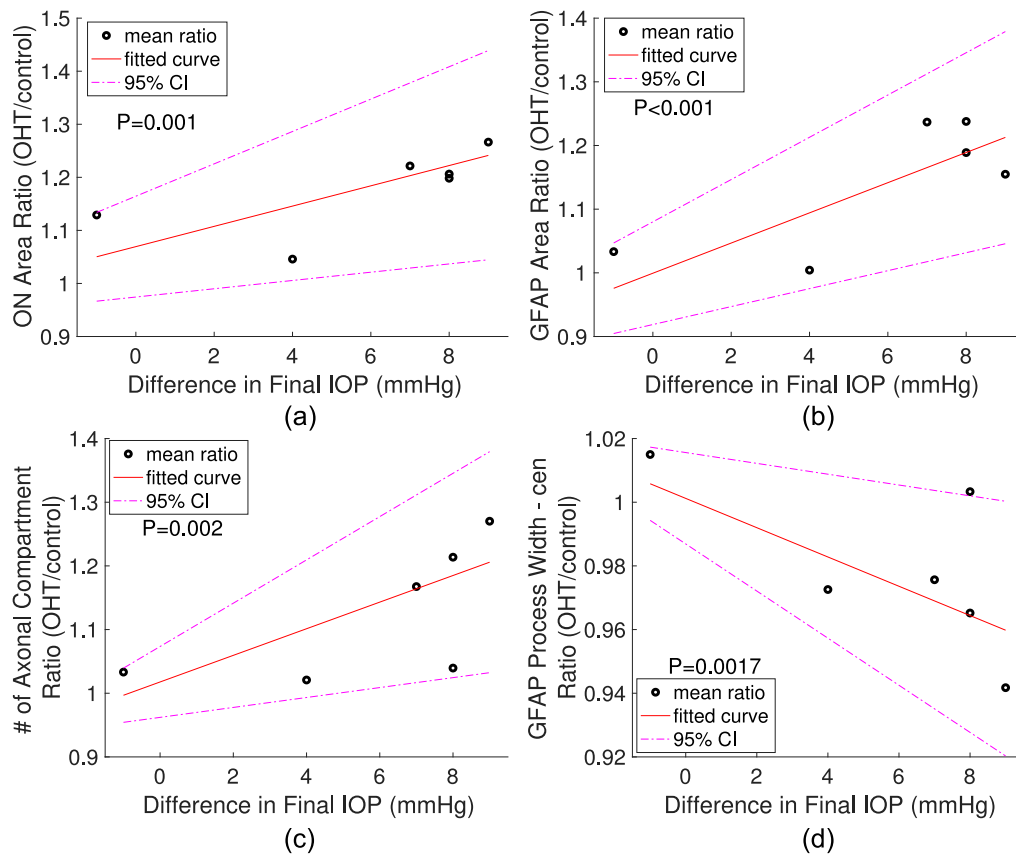
FIGURE 7. Ratios between 3-day OHT and control eye pairs for 4 parameters, calculated from each of the six 40 μm intervals in R1, were greater with larger IOP difference (ΔIOP) in (a) ON area, (b) GFAP area, and (c) number of axonal compartments, while the GFAP process width ratio was smaller with greater IOP difference. (d) Each data point represent mean of the interval ratios in R1 from each mouse. The large variations in ratios for each mouse were due to the large axial variations in R1, as shown in (Figs. 2a–2c). The correlation was analyzed using general linear models, which take into consideration correlations among repeat measurements in multiple intervals for a single ON.

represent an initial result of IOP-produced strain. The increase in actin area in R1 could be due to the extension of new fine processes[17] to separate adjoining axons that were swelling, resulting in the increase in individual axonal compartments presented in this study.

From a biomechanical perspective, the cytoskeleton provides structural properties for cells, and the expression of GFAP and actin are correlated with tissue stiffness in murine glial cells.[58–60] The initial increase in both the actin and GFAP network may serve to restore mechanical environment for axons. However, the increase in thin actin processes may not be sufficient to restore local mechanical support. This process could result in a more compliant response under pressure. Further, astrocytes in the ONH express mechanosensitive channels.[61] Larger strains experienced on the cell membrane may trigger downstream mechanically-linked signaling pathways.

The number of nuclear clusters increased dramatically, while their mean size decreased. The increase in the number of nuclei may be caused by the separation of originally overlapping nuclei. Perturbations of the intermediate filaments, which include GFAP, could alter nuclear positioning in astrocytes.[62] However, significant astrocyte proliferation has been reported by Ki67 labeling in mice 1 week after IOP elevation[46] and in rat glaucoma models.[63] Thus, some of the increase in nuclear clusters may be caused by a proliferation of astrocytes or microglia. Because external stresses are

transmitted from the plasma membrane via the cytoskeleton to the nucleus, a change in nuclear shape or conformation is expected, as we observed and has been previously reported.[64,65] The less elongated and smaller nuclear clusters could also suggest possible reorientation of the cell and nucleus toward the long axis of the nerve.

There were limitations in this study. Although GFAP served as an astrocyte-specific indicator in the ONH, phalloidin and DAPI stains are nonspecific to astrocytes. The actin area and nuclear count could include other types of cell, such as the microglia, capillary endothelium, and pericytes that are present in the ON, although they represent a small fraction of all cells. A recent study of rat ONH showed that the ON consists of 78% astrocytes.[63] The GFAP antibodies had limited depth penetration in sections, necessitating our image capture from the more superficial layer of each section. The axonal compartments were inferred from the negative space of binarized actin and nuclear images, which could include extracellular fluids or voids. The acquired signals were thresholded and binarized for quantitative measurements, potentially eliminating the variations in signal brightness and, hence, the nonuniformity of cytoskeletal proteins across the cytoplasm. However, these should not interfere with valid comparisons of the relative differences between OHT and control ON. To ensure that the images were adequately processed, the GFAP, actin, and nuclear area fractions calculated from a local region of the

binarized images were compared with that from manual tracings. The average absolute percentage difference in area fractions from the custom algorithm compared with that from the manual segmentation was 6.8%, slightly lower than the percentage difference between two manual tracings of the nuclear channels by the same operator (7.1%).

Measuring IOP at multiple time points would elucidate the total IOP exposure after bead injection. However, we only measured IOP preinjection and presacrifice to minimize the effect of repeated anesthesia exposure over the short 3-day OHT duration, which could lead to loss of some animals and a change in blood pressure, as well as a dramatic increase in physiologic stress.[66] We chose to evaluate the changes in network structure after 3 days of OHT based on previous studies of axonal transport and mechanical behavior of the astrocytic lamina. Previous studies have shown little change in axonal transport and astrocytic structure after 24 hours of IOP elevation in mouse eyes.[46] Likewise, the axonal transport obstruction was barely detectable at 24 hours, but was significant at 3 days.[7] More than 1 week of IOP elevation led to substantial axonal degeneration and represented a different phase of the remodeling process. There were also large changes in strain response after 3 days of OHT.[38] Some of the changes may be reversible if the IOP were lowered, or may progress over a longer period of time. At longer times, the remodeling of the connective tissue structure of the sclera may also alter the mechanical loading on the astrocytic lamina. We are currently developing methods to evaluate simultaneously changes in the mechanical behavior of the astrocytic lamina and peripapillary sclera of the eyes after 3 days and 6 weeks of OHT. We studied the changes in the cellular, astrocytic lamina, but are approaching alterations in the adjoining peripapillary sclera with other methods.

CONCLUSIONS

A total of 18 structural features were measured in 6 pairs of control and OHT mouse ONs. The structural features measured in cross-sections varied with axial location and region, and were correlated with degree of IOP change. Specifically, the main findings included the following.

1. There are major differences after 3 days of OHT treatment in the unmyelinated ON region, but not in the myelin transition and myelinated regions.
2. GFAP processes were thicker in the rim region compared with the central and peripheral zones. Within the unmyelinated region, processes became thinner in the central and peripheral zones after 3 days of OHT.
3. The measured ON, GFAP, actin, and nuclear areas were greater in 3-day OHT ONs in the unmyelinated region, but the GFAP area fraction was lower. The actin-labelled processes remained isotropically arranged in the cross-section after 3 days of OHT.
4. The differences between 3-day OHT and control nerves in some measured outcomes increased with larger IOP difference.

Overall, changes in the astrocytic network could affect the local biomechanical and physiologic support for retinal ganglion cell axons and may be predictive of the susceptibility to glaucomatous axonal damage.

References

1. Quigley HA, Addicks EM, Green WR, Maumenee AE. Optic nerve damage in human glaucoma: II. The site of injury and susceptibility to damage. *Arch Ophthalmol*. 1981;99:635–649.
2. Leske MC, Heijl A, Hussein M, Bengtsson B, Hyman L, Komaroff E. Factors for glaucoma progression and the effect of treatment: the early manifest glaucoma trial. *Arch Ophthalmol*. 2003;121:48–56.
3. Quigley HA, Green WR. The histology of human glaucoma cupping and optic nerve damage: clinicopathologic correlation in 21 eyes. *Ophthalmol*. 1979;86:1803–1827.
4. Gaasterland D, Kupfer C. Experimental glaucoma in the rhesus monkey. *Invest Ophthalmol Vis Sci*. 1974;13:455–457.
5. Bunt-Milam AH, Dennis MB, Bensinger RE. Optic nerve head axonal transport in rabbits with hereditary glaucoma. *Exp Eye Res*. 1987;44:537–551.
6. Morrison JC, Dorman-Pease ME, Dunkelberger GR, Quigley HA. Optic nerve head extracellular matrix in primary optic atrophy and experimental glaucoma. *Arch Ophthalmol*. 1990;108:1020–1024.
7. Kimball EC, Jefferys JL, Pease ME, et al. The effects of age on mitochondria, axonal transport, and axonal degeneration after chronic IOP elevation using a murine ocular explant model. *Exp Eye Res*. 2018;172:78–85.
8. Chidlow G, Ebneter A, Wood JPM, Casson RJ. The optic nerve head is the site of axonal transport disruption, axonal cytoskeleton damage and putative axonal regeneration failure in a rat model of glaucoma. *Acta Neuropathol*. 2011;121:737–751.
9. Voorhees AP, Jan NJ, Sigal IA. Effects of collagen microstructure and material properties on the deformation of the neural tissues of the lamina cribrosa. *Acta Biomat*. 2017;58:278–290.
10. Zhang L, Albon J, Jones H, et al. Collagen microstructural factors influencing optic nerve head biomechanics. *Invest Ophthalmol Vis Sci*. 2015;56:2031–2042.
11. Schwaner SA, Kight AM, Perry RN, et al. A methodology for individual-specific modeling of rat optic nerve head biomechanics in glaucoma. *J Biomech Eng*. 2018;140:0845011–08450110.
12. Simard M, Nedergaard M. The neurobiology of glia in the context of water and ion homeostasis. *Neurosci*. 2004;129:877–896.
13. Martin DL. Synthesis and release of neuroactive substances by glial cells. *Glia*. 1992;5:81–94.
14. Parpura V, Basarsky TA, Liu F, Jeftinija K, Jeftinija S, Haydon PG. Glutamate-mediated astrocyte-neuron signalling. *Nature*. 1994;369:744–747.
15. Sun D, Lye-Barthel M, Masland RH, Jakobs TC. Structural remodeling of fibrous astrocytes after axonal injury. *J Neurosci*. 2010;30:14008–14019.
16. Sun D, Qu J, Jakobs TC. Reversible reactivity by optic nerve astrocytes. *Glia*. 2013;61:1218–1235.

17. Wang R, Seifert P, Jakobs TC. Astrocytes in the optic nerve head of glaucomatous mice display a characteristic reactive phenotype. *Invest Ophthalmol Vis Sci*. 2017;58:924–932.

18. Hernandez MR. The optic nerve head in glaucoma: role of astrocytes in tissue remodeling. *Prog Retin Eye Res*. 2000;19:297–321.

19. Tehrani S, Davis L, Cepurna WO, et al. Astrocyte structural and molecular response to elevated intraocular pressure occurs rapidly and precedes axonal tubulin rearrangement within the optic nerve head in a rat model. *PLoS One*. 2016;11:1–22.

20. Potokar M, Kreft M, Li L, et al. Cytoskeleton and vesicle mobility in astrocytes. *Traffic*. 2007;8:12–20.

21. Tao J, Li Y, Vig DK, Sun SX. Cell mechanics: a dialogue. *Rep Prog Phys*. 2017;80:036601.

22. Pollard TD, Cooper JA. Actin, a central player in cell shape and movement. *Science*. 2009;326:1208–1212.

23. Ling YTT, Shi R, Midgett DE, Jefferys JL, Quigley HA, Nguyen TD. Characterizing the collagen network structure and pressure-induced strains of the human lamina cribrosa. *Invest Ophthalmol Vis Sci*. 2019;60:2406–2422.

24. Zhuo L, Sun B, Zhang CL, Fine A, Chiu SY, Messing A. Live astrocytes visualized by green fluorescent protein in transgenic mice. *Dev Biol*. 1997;187:36–42.

25. Regan MR, Huang YH, Kim YS, et al. Variations in promoter activity reveal a differential expression and physiology of glutamate transporters by glia in the developing and mature CNS. *J Neurosci*. 2007;27:6607–6619.

26. Cone FE, Gelman SE, Son JL, Pease ME, Quigley HA. Differential susceptibility to experimental glaucoma among 3 mouse strains using bead and viscoelastic injection. *Exp Eye Res*. 2010;91:415–424.

27. Barthel LK, Raymond PA. Improved method for obtaining 3-microns cryosections for immunocytochemistry. *J Histochem Cytochem*. 1990;38:1383–1388.

28. Zuiderveld K. Contrast limited adaptive histogram equalization. *Graph Gem*. 1994:474–485.

29. Otsu N. A threshold selection method from gray-level histograms. *IEEE Trans Syst Man Cybern*. 1979;9:62–66.

30. D'Amore A, Stella JA, Wagner WR, Sacks MS. Characterization of the complete fiber network topology of planar fibrous tissues and scaffolds. *Biomaterials*. 2010;31:5345–5354.

31. Petroll WM, Cavanagh HD, Barry P, Andrews P, Jester JV. Quantitative analysis of stress fiber orientation during corneal wound contraction. *J Cell Sci*. 1993;104:353–363.

32. Berens P. CircStat: a MATLAB toolbox for circular statistics. *J Stat Softw*. 2009;31:1–21.

33. Korneva A, Schaub JA, Jefferys JL, et al. A method to quantify regional axonal transport blockade at the optic nerve head after short term intraocular pressure elevation in mice. *Exp Eye Res*. 2020;196:108035.

34. Mabuchi F, Aihara M, Mackey MR, Lindsey JD, Weinreb RN. Optic nerve damage in experimental mouse ocular hypertension. *Invest Ophthalmol Vis Sci*. 2003;44:4321–4330.

35. Ming Lye-Barthel, Daniel Sun, Jakobs Tatjana C. Morphology of astrocytes in a glaucomatous optic nerve. *Invest Ophthalmol Vis Sci*. 2013;54:909–917.

36. Daniel Sun, Ming Lye-Barthel, Masland Richard H, Jakobs Tatjana C. The morphology and spatial arrangement of astrocytes in the optic nerve head of the mouse. *J Comp Neurol*. 2009;516:1–19.

37. Jeffery G, Evans A, Albon J, Duance V, Neal J, Dawidek G. The human optic nerve: fascicular organisation and connective tissue types along the extra-fascicular matrix. *Anat and Embryol*. 1995;191:491–502.

38. Nguyen C, Midgett D, Kimball EC, et al. Measuring deformation in the mouse optic nerve head and peripapillary sclera. *Invest Ophthalmol Vis Sci*. 2017;58:721–733.

39. Howell GR, Libby RT, Jakobs TC, et al. Axons of retinal ganglion cells are insulted in the optic nerve early in DBA/2J glaucoma. *J Cell Biol*. 2007;179:1523–1537.

40. Schaub JA, Kimball EC, Steinhart MR, et al. Regional retinal ganglion cell axon loss in a murine glaucoma model. *Invest Ophthalmol Vis Sci*. 2017;58:2765–2773.

41. Buckingham BP, Inman DM, Lambert W, et al. Progressive ganglion cell degeneration precedes neuronal loss in a mouse model of glaucoma. *J Neurosci*. 2008;28:2735–2744.

42. Anderson DR, Hendrickson A. Effect of intraocular pressure on rapid axoplasmic transport in monkey optic nerve. *Invest Ophthalmol Vis Sci*. 1974;13:771–783.

43. Minckler DS, Bunt AH, Johanson GW. Orthograde and retrograde axoplasmic transport during acute ocular hypertension in the monkey. *Invest Ophthalmol Vis Sci*. 1977;16:426–441.

44. Quigley HA, Addicks EM. Chronic experimental glaucoma in primates. II. Effect of extended intraocular pressure elevation on optic nerve head and axonal transport.. *Invest Ophthalmol Vis Sci*. 1980;19:137–152.

45. Kimball Elizabeth C, Pease Mary E, Steinhart Matthew R, et al. A mouse ocular explant model that enables the study of living optic nerve head events after acute and chronic intraocular pressure elevation: focusing on retinal ganglion cell axons and mitochondria. *Exp Eye Res*. 2017;160:106–115.

46. Quillen S, Schaub J, Quigley HA, Pease ME, Korneva A, Kimball EC. Astrocyte responses to experimental glaucoma in mouse optic nerve head. *PLoS One*. 2020;15:e0238104.

47. Korneva A, Cone-Kimball EC, Nguyen TD, Quigley HA. Regional mechanical strains in mouse astrocytic lamina and peripapillary sclera after chronic IOP elevation. *Invest Ophthalmol Vis Sci*. 2020;61:996–996.

48. Varela HJ, Hernandez MR. Astrocyte responses in human optic nerve head with primary open-angle glaucoma. *J Glaucoma*. 1997;6:303–313.

49. Etienne-Manneville S. Cytoplasmic intermediate filaments in cell biology. *Annu Rev Cell and Dev Bi*. 2018;34:1–28.

50. Johnson EC, Jia L, Cepurna WO, Doser TA, Morrison JC. Global changes in optic nerve head gene expression after exposure to elevated intraocular pressure in a rat glaucoma model. *Invest Ophthalmol Vis Sci*. 2007;48:3161–3177.

51. Qu J, Jakobs T. The time course of gene expression during reactive gliosis in the optic nerve. *Invest Ophthalmol Vis Sci*. 2013;54:5586–5586.

52. Johnson EC, Deppmeier LMH, Wentzien SKF, Hsu I, Morrison JC. Chronology of optic nerve head and retinal responses to elevated intraocular pressure. *Invest Ophthalmol Vis Sci*. 2000;41:431–442.

53. Salvador-Silva M, Ricard CS, Agapova OA, Yang P, Hernandez MR. Expression of small heat shock proteins and intermediate filaments in the human optic nerve head astrocytes exposed to elevated hydrostatic pressure in vitro. *J Neurosci Res*. 2001;66:59–73.

54. Haskin C, Cameron I. Physiological levels of hydrostatic pressure alter morphology and organization of cytoskeletal and adhesion proteins in MG-63 osteosarcoma cells. *Biochem Cell Bio*. 1993;71:27–35.

55. Girard PR, Nerem RM. Shear stress modulates endothelial cell morphology and F-actin organization through the regulation of focal adhesion-associated proteins. *J Cell Physiol*. 1995;163:179–193.

56. Ohashi K, Fujiwara S, Mizuno K. Roles of the cytoskeleton, cell adhesion and rho signalling in mechanosensing and mechanotransduction. *J Biochem*. 2017;161:245–254.

57. Hansson E. Actin filament reorganization in astrocyte networks is a key functional step in neuroinflammation resulting in persistent pain: novel findings on network restoration. *Neurochem Res*. 2015;40:372–379.

58. Lu YB, Iandiev I, Hollborn M, et al. Reactive glial cells: increased stiffness correlates with increased intermediate filament expression. *FASEB J*. 2011;25:624–631.

59. Moeendarbary E, Weber IP, Sheridan GK, et al. The soft mechanical signature of glial scars in the central nervous system. *Nat Commun*. 2017;8:1–11.

60. Maneshi MM, Sachs F, Hua SZ. Heterogeneous cytoskeletal force distribution delineates the onset Ca2+ influx under fluid shear stress in astrocytes. *Front Cell Neurosci*. 2018;12:69.

61. Choi HJ, Sun D, Jakobs TC. Astrocytes in the optic nerve head express putative mechanosensitive channels. *Mol Vis*. 2015;21:749–766.

62. Leduc C, Etienne-Manneville S. Regulation of microtubule-associated motors drives intermediate filament network polarization. *J Cell Biol*. 2017;216:1689–1703.

63. Lozano DC, Choe TE, Cepurna WO, Morrison JC, Johnson EC. Early optic nerve head glial proliferation and jak-stat pathway activation in chronic experimental glaucoma. *Invest Ophthalmol Vis Sci*. 2019;60:921–932.

64. Kim DH, Li B, Si F, Phillip JM, Wirtz D, Sun SX. Volume regulation and shape bifurcation in the cell nucleus. *J Cell Sci*. 2015;128:3375–3385.

65. Seirin-Lee S, Osakada F, Takeda J, et al. Role of dynamic nuclear deformation on genomic architecture reorganization. *PLoS Comput Biol*. 2019;15:e1007289.

66. Cone FE, Steinhart MR, Oglesby EN, Kalesnykas G, Pease ME, Quigley HA. The effects of anesthesia, mouse strain and age on intraocular pressure and an improved murine model of experimental glaucoma. *Exp Eye Res*. 2012;99:27–35.